TU Delft

Delft University of Technology

Document Version
Final published version

Licence
CC BY

Citation (APA)
Karatsu, K., Endo, A., Dabironezare, S., Murugesan, V., Thoen, D. J., Olde Scholtenhuis, L. G. G., Rybak, M., Steenvoorde, F., Baselmans, J. J. A., & More Authors (2026). DESHIMA 2.0: A 200–400 GHz ultra-wideband integrated superconducting spectrometer. *Astronomy and Astrophysics*, *712*, Article A12. https://doi.org/10.1051/0004-6361/202658904

Important note
To cite this publication, please use the final published version (if applicable).
Please check the document version above.

Copyright
In case the licence states “Dutch Copyright Act (Article 25fa)”, this publication was made available Green Open Access via the TU Delft Institutional Repository pursuant to Dutch Copyright Act (Article 25fa, the Taverne amendment). This provision does not affect copyright ownership.
Unless copyright is transferred by contract or statute, it remains with the copyright holder.

Sharing and reuse
Other than for strictly personal use, it is not permitted to download, forward or distribute the text or part of it, without the consent of the author(s) and/or copyright holder(s), unless the work is under an open content license such as Creative Commons.

Takedown policy
Please contact us and provide details if you believe this document breaches copyrights.
We will remove access to the work immediately and investigate your claim.

This work is downloaded from Delft University of Technology.

A&A, 712, A12 (2026)
https://doi.org/10.1051/0004-6361/202658904
© The Authors 2026

Astronomy & Astrophysics

DESHIMA 2.0: A 200–400 GHz ultra-wideband integrated superconducting spectrometer

K. Karatsu[1,⋆], A. Endo[2], A. Moerman[2], S. J. C. Yates[1], R. Huiting[1], A. Pascual Laguna[3], S. Dabironezare[1,2], V. Murugesan[1], D. J. Thoen[1], B. T. Buijtendorp[2], S. Cray[4], K. Fujita[5], S. Hähnle[2], S. Hanany[4], R. Kawabe[6], K. Kohno[7,8], L. H. Marting[2], T. Matsumura[9], S. Nakatsubo[10], L. G. G. Olde Scholtenhuis[2], T. Oshima[6], M. Rybak[2,11], F. Steenvoorde[2], R. Takaku[9], T. Takekoshi[12], Y. Tamura[13], A. Taniguchi[12,13], P. P. van der Werf[11], and J. J. A. Baselmans[1,2,14]

(Affiliations can be found after the references)

Received 9 January 2026 / Accepted 6 June 2026

ABSTRACT

Context. The Deep Spectroscopic HIgh-redshift MApper (DESHIMA) is a broadband integrated superconducting spectrometer for millimeter (mm) and submillimeter (submm) wave astronomy based on kinetic inductance detectors (KIDs). The first generation, DESHIMA 1.0, was successfully tested in 2017. This paper describes the upgrade to DESHIMA 2.0 and presents its characterization in laboratory settings.

Aims. We enhanced the performance by increasing the band coverage and efficiency while developing a fast sky-position chopper for the efficient removal of atmospheric fluctuations.

Methods. The instrument features NbTiN superconducting microstrip (MS) filters with a low-loss a-SiC:H dielectric and an ultra-wideband leaky-wave antenna. A laboratory setup was designed, incorporating the cryostat housing cryogenic optics and integrated superconducting spectrometer chip comprising 339 KIDs connected to MS filters tuned for (sub)mm wave frequencies. Room-temperature mirrors on a hexapod stage allowed us to precisely position and align the optical elements. The sky-position chopper was positioned on a motor-controlled stage for a fine-tuned control over its position and alignment. The multiplexing capability of KIDs enabled us to simultaneously measure multiple performance metrics across the entire frequency range.

Results. DESHIMA 2.0 achieved significant improvements in the performance compared to its predecessor: the measured instantaneous frequency coverage was 200–400 GHz with a mean filter Q_{filter} of 340 ± 50, the instrument efficiency reached ∼8%, indicating a four times wider band coverage and a four times higher sensitivity. The yield rate for the MS filters exceeded 98%. The data loss caused by the sky-position chopper was limited to <20% without beam truncation. The estimated aperture efficiency from measured beam patterns agreed well with the designed value of approximately 70%. The telescope far-field beam patterns calculated from the measured patterns also agree well with the design specifications. We also demonstrated that a new method of absolute frequency calibration is valid using the data from the beam pattern measurement.

Key words. instrumentation: detectors – instrumentation: spectrographs – techniques: spectroscopic

1. Introduction

As millimeter (mm)/submillimeter (submm) wave astronomy continues to evolve, there has been an increasing need for compact and wide-band spectrometers. To meet this requirement, significant progress has been made in developing instruments using integrated superconducting spectrometer (ISS), such as DESHIMA (Deep Spectroscopic HIgh-z MApper, Endo et al. 2019a; Taniguchi et al. 2022), Superspec (Karkare et al. 2020), μ-spec (Mirzaei et al. 2020), and SPT-SLIM (Karkare et al. 2022). DESHIMA is a broadband spectrometer with a moderate frequency resolution (R = 100–1000). By integrating superconducting resonant filters and kinetic inductance detectors (KIDs, Day et al. 2003), DESHIMA embodies the concept of the ISS: The high multiplexing capability of KIDs enables an on-chip filterbank architecture, where each signal from an individual filter is read out by a corresponding KID. This design allows us to efficiently and simultaneously measure multiple frequency channels across the (sub-)mm wave spectrum. Importantly, the ISS technology is scalable to an integrated field unit (IFU) by increasing the number of spatial pixels to ≳100.

The first generation of DESHIMA (DESHIMA 1.0, Endo et al. 2019a), covering the frequency range of 332−377 GHz with a filter resolution (Q_{filter}) of ∼300 and an instrument efficiency of ∼2%, was successfully tested on the Atacama Sub-millimeter Telescope Experiment (ASTE) telescope in 2017 (Endo et al. 2019b).

We describe DESHIMA 2.0, the successor of DESHIMA 1.0. DESHIMA 2.0 is an on-chip filterbank spectrometer with an instantaneous band of 200−400 GHz and a design spectral resolution ($\Delta F/F$) of 500. In DESHIMA 2.0, we use 339 KIDs that are read out using a single back end within a 2–4 GHz bandwidth. Hence, it covers a sky bandwidth of ∼200 GHz with a readout bandwidth of 2 GHz. The separation between signal bandwidth and readout bandwidth makes the on-chip spectrometers very resource efficient compared to

⋆ Corresponding author: k.karatsu@sron.nl

Open Access article, published by EDP Sciences, under the terms of the Creative Commons Attribution License (https://creativecommons.org/licenses/by/4.0), which permits unrestricted use, distribution, and reproduction in any medium, provided the original work is properly cited.
This article is published in open access under the Subscribe to Open model. Subscribe to A&A to support open access publication.

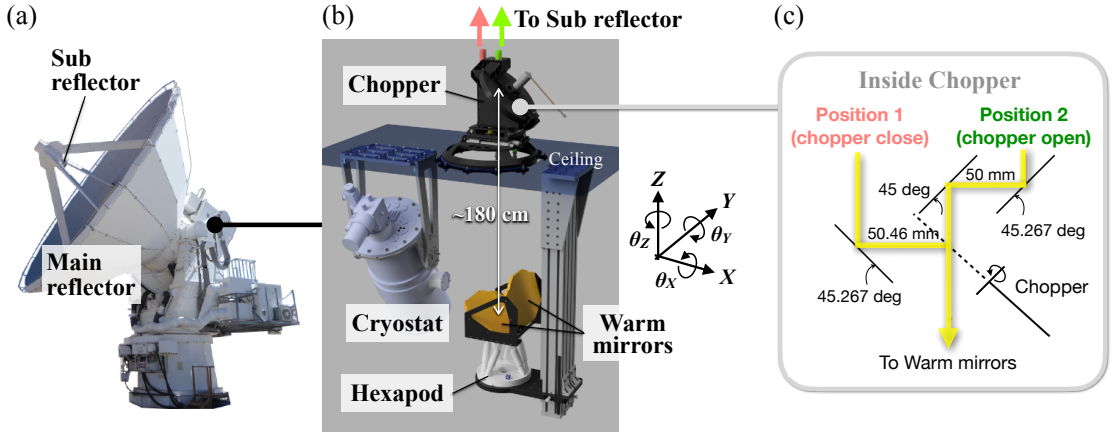


Fig. 1. (a) ASTE telescope, whose main reflector has a diameter of 10 m. It is located at an altitude of 4860 m altitude on Pampa la Bola in the Atacama desert, Chile. (b) Setup inside the ASTE cabin. The location of the sky-position chopper is ~180 cm above the warm mirrors. The red and green arrows correspond to the two different beam positions (positions 1 and 2) shown in panel (c). (c) Schematic drawing of the inside of the chopper. The two beams at positions 1 and 2 are separated by 100.46 mm and reflected by mirrors with a tilt angle of 45.267° to create a 234 arcsec pointing separation on the sky.

heterodyne/coherent systems, which require faster readout electronics with multiple instrument tunings to cover the same sky frequency band.

The primary science target of DESHIMA 2.0 is to study the cosmic history of star formation and galaxy evolution by detecting molecular and atomic emission lines from bright dusty star-forming galaxies at high redshifts (Rybak et al. 2022). The moderate frequency resolution of 500 is designed to match the typical line velocity width of the most massive dusty star-forming galaxies ($\Delta\upsilon$ = 600 km/s, Carilli & Wang 2006). The broadband feature also enables us to probe the dynamics of galaxy clusters through spectroscopic observations of the Sunyaev–Zel'dovich effect (Sunyaev & Zeldovich 1970, 1980).

Compared to DESHIMA 1.0, DESHIMA 2.0 offers broader frequency coverage and enhanced sensitivity by combining an ultra-wideband leaky-wave antenna (Neto 2010; Neto et al. 2010; Hähnle et al. 2020, Dabironezare et al., in prep.) and an NbTiN superconducting micro-strip (MS) filterbank spectrometer (Pascual Laguna et al. 2021; Thoen et al. 2022) with low-loss a-SiC:H dielectric (Buijtendorp et al. 2022, 2025). The DESHIMA 2.0 instrument also features a fast sky-position chopper that enables a more efficient removal of atmospheric fluctuations than its predecessor, resulting in longer on-source time fractions. Finally, it features a higher transmission optics, in particular, the antireflection (AR) coated cryostat window and infrared filters. The DESHIMA 2.0 instrument was deployed to the ASTE telescope in 2023, and we carried out a one-year-long on-sky campaign (Moerman et al. 2025, Endo et al., in prep.).

The design of the DESHIMA 2.0 instrument and the full characterization of the instrument in the laboratory are described in this paper. The paper structure is as follows: We explain the specification of the DESHIMA 2.0 instrument in Sect. 2.1 together with its cryogenic configuration. Sect. 2.2 describes details of the ISS chip of DESHIMA 2.0. Then, in Sect. 2.3, we discuss the laboratory setup and experiments we performed to characterize the instrument. In Sects. 3.1, 3.2, and 3.3, we show the results of the on-chip filter characterization, the instrument sensitivity, and the beam characteristics of the DESHIMA 2.0 instrument, respectively. We show in Sect. 3.4 the result of the absolute frequency calibration of the instrument that we obtained by comparing filter responses with output frequencies from the harmonic mixer that was used in the beam pattern measurements. Finally, Sect. 4 concludes the paper.

2. Methods

2.1. The DESHIMA 2.0 instrument

The DESHIMA 2.0 instrument was designed to fit in the ASTE telescope (Figs. 1a, b). Figure 1b shows the interior of the ASTE cabin with the DESHIMA 2.0 instrument. It consists of three main components: (1) a sky-position chopper with a motor-controlled stage, (2) room temperature warm mirrors supported by a hexapod, and (3) the cryostat housing the DESHIMA ISS chip together with the cryogenic optics. All of these are attached to the ceiling of the ASTE cabin, thereby creating a stable relative position between these three components and a first-order absolute alignment. The ISS in the cryostat, the telescope optics, and the beam modulator are precisely aligned optically with the motor-controlled stage of the sky position chopper and the hexapod. This is discussed in detail in Moerman et al. (2024).

The sky-position chopper consists of three planar mirrors and a wheel. Figure 1c displays a schematic drawing of the inside of the chopper. The optical pass through the chopper changes by rotating the wheel (denoted as positions 1 and 2 in Fig. 1c). The chopper wheel rotates at a frequency of 5 Hz, resulting in a chopping frequency of 10 Hz with a duty cycle close to 50% because the wheel has two slots, each of which occupies a quarter of the surface area of the wheel. In order to monitor the phase (slot or open) of the wheel, a diode sensor is installed inside the chopper module. The chopping frequency is set not only to remove atmospheric fluctuation (order of <1 Hz), but also to suppresses the 1/f noise due to the two-level system (TLS) noise in the KIDs (Gao et al. 2008). The chopper is positioned on a motor-controlled stage, whose travel range is ±25 mm in the X/Y direction with 10 μm accuracy (the definition of the coordinates is shown in Fig. 1b). Two beams from positions 1 and 2 illuminate the sub-reflector of the ASTE telescope with a separating distance of ~100 mm, resulting in a ±117 arcsec pointing offset along the azimuthal direction with respect to broadside. The azimuthal offset is chosen to be large enough compared with the beam size of the ASTE telescope over the DESHIMA 2.0 frequency band of 200–400 GHz, and, at the same time, to be small

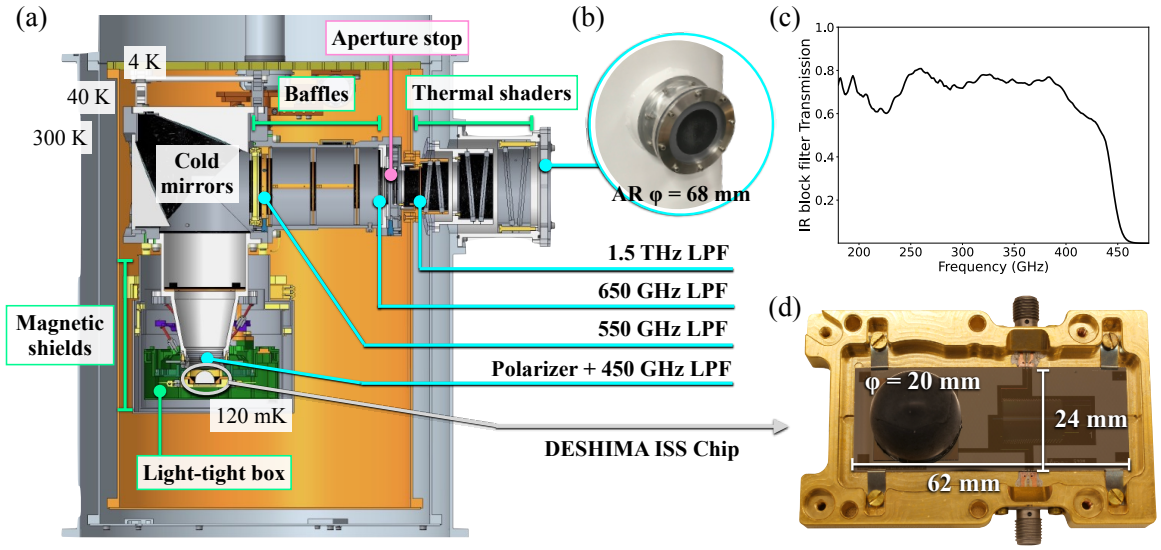


Fig. 2. (a) Cross-section and overview of the DESHIMA cryostat with explanations of components. (b) Si vacuum window with laser-ablated AR structures. (c) Total transmittance of the Si window, thermal shaders, and IR-blocking filters along the cryogenic optical throughput. Four types of IR blocking filters (1.5 THz low-pass filter (LPF), 650 GHz LPF, 550 GHz LPF, and 450 GHz LPF) are installed in the optical throughput. (d) DESHIMA 2.0 spectrometer (ISS) chip.

enough to see the same patch of atmosphere for effective removal of the atmospheric fluctuation.

The two warm mirrors consists of a hyperboloidal mirror and an ellipsoidal mirror. They are placed in a modified Dragonian configuration (Dragone 1978). The mirrors are inside a single rigid support structure that is mounted onto a six-axis motorized hexapod. The travel range of the hexapod is ±50 (25) mm in the X/Y (Z) direction with an accuracy of 4 μm, and the rotation range is ±15° (30°) in θ_X/θ_Y (θ_Z) with an accuracy of 7.5 μrad.

Figure 2a displays an overview of the DESHIMA cryostat, which is the same two-stage adiabatic demagnetization refrigerator (ADR; Entropy GmbH) as was used for DESHIMA 1.0 (Endo et al. 2019a). The cryostat has a 6 mm thick silicon (Si) vacuum window that is AR coated with a laser-ablated sub-wavelength structure over its central 68 mm diameter (Fig. 2b). The transmittance of the window exceeds 95% over the frequency band of DESHIMA 2.0 (Takaku et al. 2026). Along the optical path inside the cryostat, thermal shaders and infrared (IR) blocking filters are installed, as well as baffles coated by a radiation absorber (Klaassen et al. 2001) to limit large angular stray radiation. Figure 2c shows the total transmittance of the combination of Si window, thermal shaders, and IR blocking filters as a function of frequency, showing that an average transmission of 70% is achieved over the frequency band of DESHIMA 2.0. This is higher than the filters and window for DESHIMA 1.0, which was ∼40% (Endo et al. 2019a). The cold mirrors consist of a parabolic relay with two off-axis paraboloid reflectors that are mounted on the 4 K stage as one unit. The cryogenic optics couple the radiation entering the cryostat to the ISS chip, which is located at 120 mK stage inside the light-tight box (Baselmans et al. 2012). The light-tight box, which holds the detector chip, is thermally anchored to the cold stage of the ADR and is operated at 120 mK. It is surrounded by dual-layer magnetic shield of Nb and Cryoperm, cooled to 4 K. The thermal isolation between the 4 K optics box and the 120 mK light-tight box is achieved using a thermal-mechanical assembly identical to the one used by DESHIMA 1.0, which is based upon vespel rods and in-house made thermal straps. It uses an intermediate thermal stage, connected to the 0.8 K stage of the ADR, to reduce the heat load on 120 mK, which is also used to thermalize the coax cables used for the readout. Figure 2d shows the DESHIMA ISS chip with its holder. It is equipped with a Si lens of 20 mm diameter, which is AR coated with a ∼120 μm thickness of a mixture of Stycast 2850FT and 1266A to make a reflective index n = 1.84 (Suzuki et al. 2012; Nitta et al. 2014). The lens is placed at a distance of 10 μm from the leaky-wave antenna feed that connects to the filterbank. The lens-antenna and cold and warm optics provide a highly efficient radiation coupling over a the full DESHIMA 2.0 band (described in detail by Dabironezare et al., in prep.). In front of the lens, a polarizer is also mounted to select the polarization of the incoming radiation. The detailed design of the ISS chip is described in the next section (Sect. 2.2).

The ISS chip is connected to the cryogenic readout chain by a pair of coax lines. A low-noise amplifier with +26 dB gain and noise temperature of ∼2 K (Low Noise Factory; LNF-LNC1.5_6A s/n 750B) is located at the 4 K stage in the output line of the readout chain. The readout signal is further amplified right after the exit of the cryostat by an amplifier with +20 dB gain. The readout chain is connected to a room-temperature frequency-division multiplexing readout system (van Rantwijk et al. 2016) to read out the response of all KIDs simultaneously. The sampling speed of the readout system can be selected from ∼160 Hz or ∼1.3 kHz, and we used both settings depending on the requirements from experiments.

The total loading power, including the power from the optical throughput, the mechanical support structure, and the readout chain, was measured to be ∼2 μW at the coldest stage. With the operation temperature of 120 mK, we measured a hold time of the ADR of more than 24 hours.

2.2. The DESHIMA 2.0 ISS chip

The size of the DESHIMA 2.0 ISS chip is 62 mm × 24 mm, as shown in Fig. 2d. It is fabricated from a 350 μm FZ < 100 > Si wafer with ρ > 10 kΩcm coated on both sides by a 1 μm low-pressure chemical vapor deposition (LPCVD) Si-rich SiN

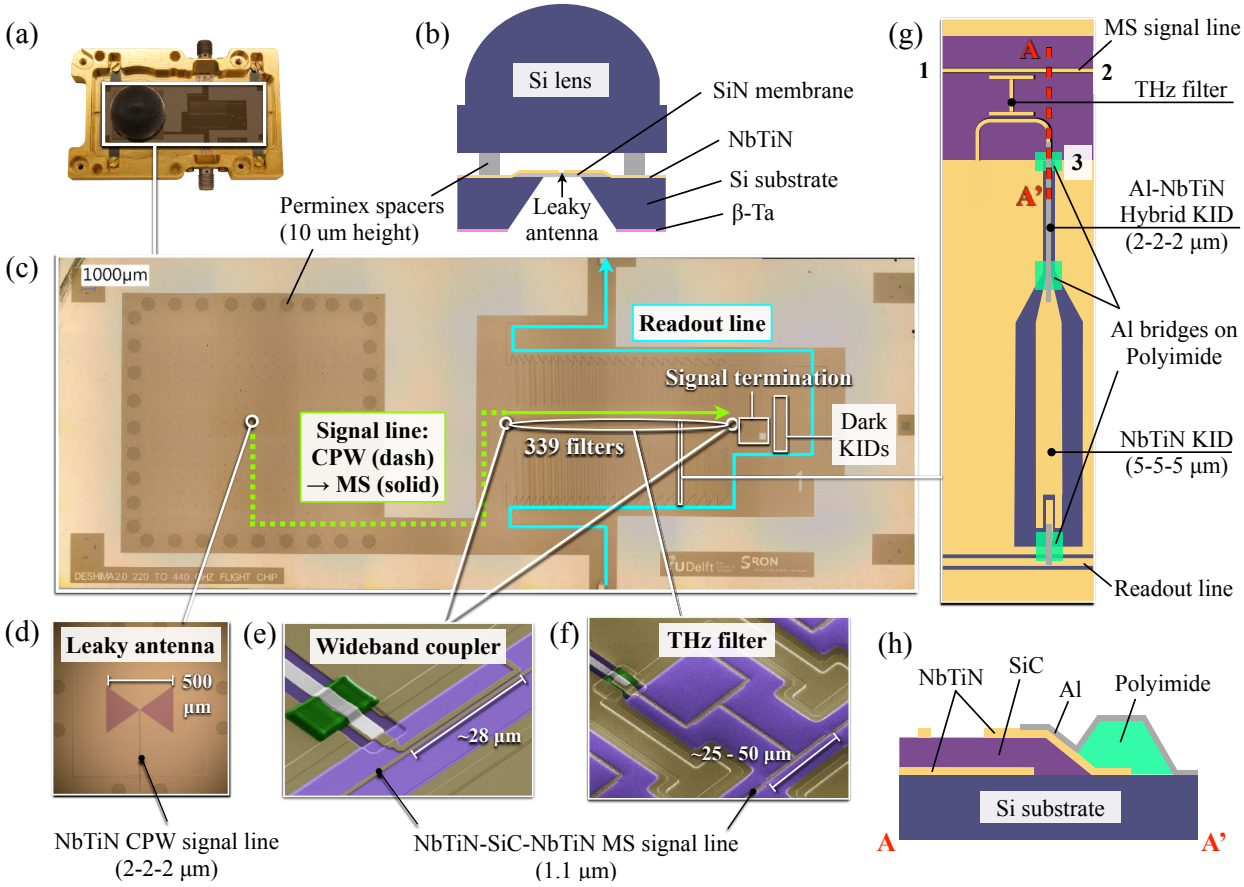


Fig. 3. (a) Photograph of the DESHIMA 2.0 spectrometer chip with its holder. The white rectangle indicates the spectrometer chip, which is shown zoomed in (c). (b) Cross-section around the Si lens and the antenna (not to scale). (c) Micrograph of the spectrometer chip. The location of the leaky-wave antenna, the signal line, the wideband couplers, the THz filters (filterbank), the signal termination, dark KIDs and the readout line are indicated. The Perminex spacers with a height of 10 μm around the antenna are also shown. (d) Zoomed-in micrograph of the leaky-wave antenna on the SiN membrane. The antenna width is 500 μm, and it has a CPW-based quarter-wave impedance-matching structure that eventually connects to the NbTiN CPW signal line with a geometry of 2–2–2 μm. (e) Colored SEM image of the wideband coupler. The coupler length is ~28 μm, and it is weakly coupled to the MS signal line of 1.1 μm width. The coupling strength is designed to be −29 ± 1 dB over the frequency range of DESHIMA 2.0. (f) Colored SEM image of the THz filter (image taken from Thoen et al. 2022). The filter coupler length varies from ~25–50 μm depending on the resonance frequency of the filter. The distance between the filter and the signal line is designed to be 300 nm. In the filterbank, the spectral channels are placed in decreasing order of frequency from 400 GHz to 200 GHz. (g) Schematic drawing of a pair of MS THz filter and KID, showing how each component is connected or coupled. KID consists of a short-ended NbTiN MS line with a width of 1.5 μm that couples to the filter NbTiN-Al hybrid CPW line with a geometry of 2–2–2 μm and to the open-ended NbTiN CPW line with a geometry of 5–5–5 μm. Al bridges are used to electrically connect the NbTiN MS line, the NbTiN-Al hybrid CPW line, and the NbTiN CPW line of the KID. The open end of the KID is capacitively coupled to the CPW readout line with an Al bridge. Not displayed in the drawing, Al bridges are also used to balance the ground planes of the readout CPW line by placing them in a random spacing. (h) Cross-section of the connection between the MS line and the Al line of the hybrid CPW (not to scale). The corresponding location is indicated by the dashed red line in panel (g).

layer with a (tensile) stress $\sigma \approx +150$ MPa. This layer is removed everywhere using reactive ion etching (RIE), except on the wafer front side, where the antenna will be located. We used a plasma with 13.5 sccm Ar^+ and 25 sccm O_2 at 50 W and 5 mTorr, followed by a 90 second pure O_2 descum, to create a sloped edge on the SiN to facilitate the later step coverage.

The second layer is the NbTiN ground, deposited using shuttled reactive magnetron sputtering from a NbTi target in an argon-nitrogen plasma to deposit a very flat 200 nm NbTiN layer (Thoen et al. 2017) with a $T_c = 14.7$ K that is also patterned using the same sloped-edge RIE process to create the ground plane of the MS filterbank.

The third layer is the filterbank dielectric, fabricated from a 500 nm thick a-SiC:H deposited at 400 °C using plasma-enhanced chemical vapor deposition (PECVD) (Buijtendorp et al. 2022). We again used the sloped-edge RIE process to pattern the a-SiC:H, which is smaller than the NbTiN ground plane almost everywhere, to create a good galvanic connection with the next NbTiN top layer, as shown in panels e and f of Fig. 3. However, where the KIDs connect to the filters, only the KID central line needs to be connected to the NbTiN top layer, so here, the a-H:SiC is patterned to overlap the NbTiN ground, as shown in panels g and h of Fig. 3.

The fourth layer is defined from a 207 nm NbTiN layer, identical to the ground-plane layer. We used a dual e-beam/UV exposure of ma-N1405 negative tone resist, which is sensitive to the 365 nm UV radiation from our UV mask aligner and to the 100 keV electrons from our electron beam pattern generator (EBPG). The mask aligner is used to expose the large ground planes and coarse structures, and the EBPG is used to define the signal line and the KID couplers. The details of this mix-and-match fabrication are described in Thoen et al. (2022).

After development, the NbTiN was etched in the RIE using a recipe with less oxygen to create steeper slopes and a better edge definition: we used a 25 sccm Ar – 13.5 sccm O_2 plasma at 50 W and 5 mTorr, followed by a 90 second pure O_2 descum.

The fifth layer consists of a 500 nm thick polyimide, which is photosensitive and patterned into small rectangles to support the aluminum (Al) of the bridges over the readout line and to the KID couplers.

The sixth layer is a 35 nm thick aluminum (Al) (T_c = 1.2 K), which is used as radiation absorber in the NbTiN–Al hybrid KIDs (Janssen et al. 2013; Baselmans et al. 2017) and for the Al bridges. This Al is sputter-deposited using shuttling with the same target dimensions and method as the NbTiN layers (Thoen et al. 2017) to create a very flat Al layer. This layer is patterned in two steps: first, we performed a normal UV exposure and wet etching to define the bridges and the Al in the KIDs, with the latter a few micron wider than their final dimension. In the next step, we used PMMA, EBPG patterning and wet etching to very accurately define the final Al linewidth. The use of very flat NbTiN and Al layers and the EBPG patterning of the filters and KID Al is key in reducing frequency scatter of the KIDs and filters, as we show below.

The seventh layer is 10 µm Perminex (KAYAKU PermiNex 1010), deposited using spin coating, UV exposure, and developing. This material is used to define the vacuum gap at the leaky-wave antenna and glue the Si spacer-Si lens to the chip, similar as in Baselmans et al. (2022). When all these layers were patterned, we used KOH etching to remove the Si behind the SiN with the leaky-wave antenna feed to create a free-standing membrane.

The final layer is a 40 nm β-phase Ta ($T_c \sim 0.7$ K) deposited on the backside of the chip as an absorbing mesh for stray-light control (Yates et al. 2017). This layer was created using sputter deposition, UV patterning, and dry etching. We used careful resist placement and spinning to prevent resist from filling up the holes in the Si at the positions of the SiN membranes.

Figure 3a shows the same picture as Fig. 2d, but the DESHIMA ISS chip is indicated, whose micrograph is shown in Fig. 3c. Figure 3b displays a schematic drawing of the cross-section around the Si lens and the antenna (not to scale). The Si lens is fixed and supported by 10 µm high Perminex pillars on the chip. The Si lens and antenna were aligned using the alignment marker patterned at the center of the Si lens and the center of the antenna. The linearly polarized incoming radiation that enters through the Si lens is received by the broadband leaky-wave antenna on the SiN membrane (Fig. 3d). The received signal is guided to the filterbank through the coplanar waveguide (CPW) signal line that is converted into an MS line right before entering the filterbank, as indicated by the light green lines in Fig. 3c (CPW part: dashed line, MS part: solid line). The signal is then sorted into 339 spectral channels over the ∼200–400 GHz frequency range of DESHIMA 2.0 by 339 narrow-bandpass half-wavelength MS filters (called THz filter hereafter, Pascual Laguna et al. 2021) in the filterbank. The separation of the neighboring filters of the resonance frequencies of F^i_{filter} and F^{i+1}_{filter} (i denotes the ith filter) is designed as $\lambda^i_{eff}/4 = c/(4F^i_{filter}\sqrt{\varepsilon_{eff}})$, where c is the speed of light in free space, and $\varepsilon_{eff} \sim 30$ describes the effective phase velocity of the MS line, $v_{ph} = c/\sqrt{\varepsilon_{eff}}$, including the permitivity of the dielectric and the kinetic inductance of the NbTiN. As a reference for the incoming signal power, four wideband couplers are placed, two before and two after the filterbank. They are weakly coupled to the signal line. The separation of the wideband couplers is $\lambda_{eff}/4$ at 300 GHz, which is the center frequency of the DESHIMA 2.0 band. In this way, the effect of a possible standing wave in the signal line can be canceled when responses of the KIDs connected to the two wideband couplers are coadded (before the filterbank). The details of how these wideband couplers were used in the analysis are described in Sect. 3.1. Figures 3e and f show colored scanning electron microscope (SEM) images of the wideband coupler and the THz filter, respectively. Figure 3g displays a schematic drawing of a pair of THz filters and the corresponding KID. The MS filter is coupled to the MS signal line on one side and to a KID on the other side. The KID is a quarter-wavelength hybrid resonator (Janssen et al. 2013), consisting of a short-ended NbTiN MS line that couples to the filter, NbTiN–Al hybrid CPW line, and open-ended NbTiN CPW line. We used a polyimide support wherever we need to galvanically connect Al to NbTiN to prevent yield issue due to trenching. The open end of the KID is capacitively coupled to the CPW readout line via a coupling structure that is galvanically connected to the readout line by such an Al-polyimide bridge. Figure 3h shows a schematic drawing of the cross-section of the connection between the MS line and the Al line of the hybrid CPW (not to scale; the corresponding location is indicated by the dashed red line A–A′ in Fig. 3g). After the filterbank, the signal line is terminated by a CPW line with an Al center line to absorb the remaining signal, which prevents reflection of power that is not absorbed by the filter channels. In the chip, four dark KIDs, not connected to filters or coupled to the signal line, are placed at the location away from the signal line to measure the power level of stray light or surface waves in the substrate. The locations of the signal termination and dark KIDs are also shown in Fig. 3c. All KIDs are coupled to one readout line, and the microwave resonance frequencies are designed to be distributed within a range of 4–6 GHz with a step of Δf_r = 4.5 MHz. The in-band power coupled to an individual MS filter is absorbed in the Al of the hybrid CPW, changing the surface impedance and hence the resonant frequency of the KID. The shift of the resonance frequency is read out as a change in the transmission amplitude and phase of a microwave tone in the readout line.

2.3. Setup and experiments in the laboratory

In order to characterize the DESHIMA 2.0 instrument, we created a 1 : 1 copy of the telescope cabin in our laboratory in which the three main components (sky chopper, warm mirrors, and cryostat) of the instrument were located at the same relative positions as inside the telescope cabin. For practical reasons, we rotated the entire system by 90 degrees so that the warm mirrors and the sky chopper were positioned horizontally, as shown in Fig. 4. We placed the warm mirrors and chopper each on a separate small optical table and used mechanical locks to create a rough alignment that was extremely reproducible. This allowed us to efficiently test the subsystem by removing one or two optical tables. All distances were identical to the telescope cabin situation. After the relative positions were roughly fixed, precise positioning and alignment were made with the motor-controlled stage attached to the sky chopper and the hexapod attached to the warm mirrors. This strategy is identical to the telescope cabin.

We carried out a series of experiments to characterize the DESHIMA 2.0 instrument as follows:

Step 1: we measured the frequency response of all THz filters at the measurement plane (MP) 1 in front of the cryostat window, as indicated in Fig. 4. This was done using a continuous wave (CW) frequency source.

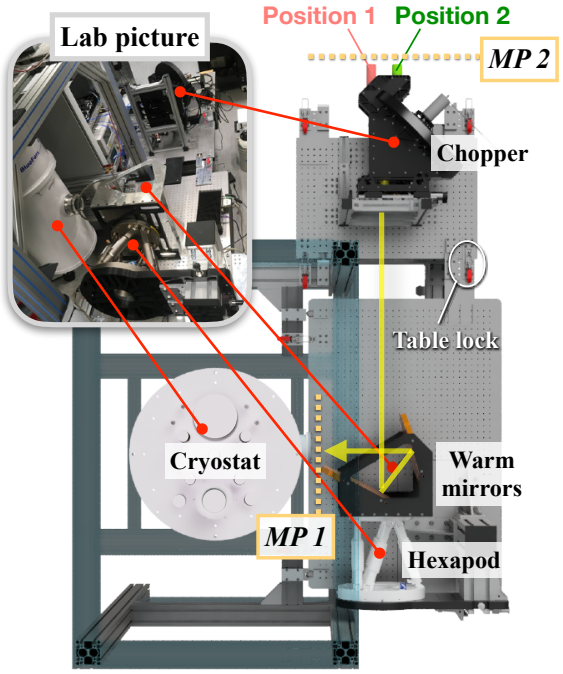


Fig. 4. Rendered CAD drawing of the laboratory setup with the inset picture of the laboratory setup. The red lines correspond each component of the instrument in the laboratory picture to the rendered drawing. The optical path from the sky chopper to the cryostat is shown as the yellow arrow. The definition of two measurement planes (MP1 and 2) is indicated as yellow dashed lines.

Step 2: we measured the beam patterns at MP 1 to verify the phase and amplitude (PA) beam patterns in front of the cryostat window.

Step 3: after aligning the warm mirrors and the chopper positions with respect to the cryostat, we measured the beam patterns at MP 2, which was after the chopper module, as indicated in Fig. 4. The beam patterns of the two optical paths (positions 1 and 2) of the chopper were measured separately by fixing the chopper position at either position.

Step 4: we measured the instrument noise equivalent power (NEP_{inst}) and optical coupling efficiency (η_{inst}) at MP 2 to evaluate the optical sensitivity of the instrument. This measurement cannot be done without a proper alignment in Step 3. We took data in two configurations: T_{cold} at position 1, and T_{room} at position 2, and vice versa, in order to characterize the two optical paths separately.

The alignment in step 3 was made by simulating the warm mirrors and hexapod and performing a ray-tracing analysis through the warm mirrors to calculate the optimal hexapod configuration using the beam patterns obtained in step 2 as input. The ray-tracing calculations and simulations of the warm optics were made using the optical simulation software PyPO (Moerman et al. 2023). The alignment procedure (steps 2 and 3) is described in detail by Moerman et al. (2024). Step 3 also involved some iterations to obtain correct information of the relative position between the optical components and the measurement planes (MP 1 and 2) in the real setup in order to properly implement MP 1 and 2 in the simulation. This was not only to improve the alignment quality, but was also essential to propagate the measured beam patters through a model of ASTE using a physical optics calculation, which is also supported by PyPO, to estimate the expected performance of the instrument at the telescope.

In above experiments, the changes in the transmission amplitude and phase of microwave tones, tuned to each KID, were read out when taking time domain data. We also read out several microwave tones that were off from the KID frequencies (called blind tones) to measure the readout electronics noise. In the data analysis, we converted the phase change ($\delta\theta$) into the microwave frequency response ($x \equiv (f - f_r)/f_r = \delta f/f_r$, where f_r represents resonance frequency of the KID) by using the KID phase versus frequency dependence curve obtained from so-called the local sweep measurement (Bisigello et al. 2016). In the local sweep measurement, the frequency of the microwave tones were locally swept in a range of 2 MHz with 10 kHz steps by sweeping the frequency of the local oscillator used in the readout system, so that we were able to measure the complex S_{21} transmission parameters of all KIDs simultaneously and extract KID parameters such as f_r and Q_r by a Lorentzian fit of the measured S_{21} (Gao 2008). The local sweep data were obtained every time before the measurement of time-domain data.

3. Results and discussions

In this section, we first present the THz filter characteristics from step 1 in Sect. 3.1. We then show the optical sensitivity of the instrument from step 4 in Sect. 3.2. In Sect. 3.3, we describe the expected beam characteristics at the telescope, calculated using PyPO, by propagating the measured phase and amplitude (PA) beam patterns from step 3. Finally, the result of the absolute frequency calibration using the results from steps 1 and 3 is presented in Sect. 3.4.

3.1. THz filter characteristics

To measure the frequency response of THz filter, we used a photo-mixing THz CW source (Toptica, Terabeam 1550) mounted on a third optical table (not shown in Fig. 4), directly in front of the cryostat window. It can emit a signal in the frequency range of 100 GHz to 1.2 THz with a relative frequency accuracy of 20 MHz. The signal power of the CW source was modulated by 12 Hz and so modulated the detector response in time domain. We carried out the experiment with a sampling frequency of ~160 Hz, which is high enough to trace the 12 Hz modulation. By sweeping the frequency of the CW source from 180 GHz to 460 GHz in 50 MHz step, we measured the response of all KIDs simultaneously, based on which, we characterised THz frequency response of each filter. This allowed us to correlate the KID readout frequency to an individual THz filter frequency and compare both to the designed values more details of the experiment were described in Endo et al. (2019a). The absolute frequency accuracy of the CW source was 2 GHz, so that another measurement was required for the absolute frequency calibration of the THz filter frequency. This is discussed in Sect. 3.4.

Figure 5a shows the frequency response of the DESHIMA 2.0 ISS, which is defined as the response of the KID at filter i, caused by the power at port 3 in Fig. 3g entering the KID due to a THz signal at port 1 (see Fig. 3g) entering the filter bank. This is defined as S_{31}, given by (Pascual Laguna et al. 2021)

$$\left|S^i_{31}(F)\right|^2 = \frac{x^i_{filter}(F)\,(dx^i_{filter}/dP^i_{abs})^{-1}}{x_{wb,bf}(F)\,(dx_{wb,bf}/dP^{wb,bf}_{abs})^{-1}}\,\eta_{wb,bf} \tag{1}$$

$$\sim \frac{x^i_{filter}(F)}{x_{wb,bf}(F)}\,\eta_{wb,bf}, \tag{2}$$

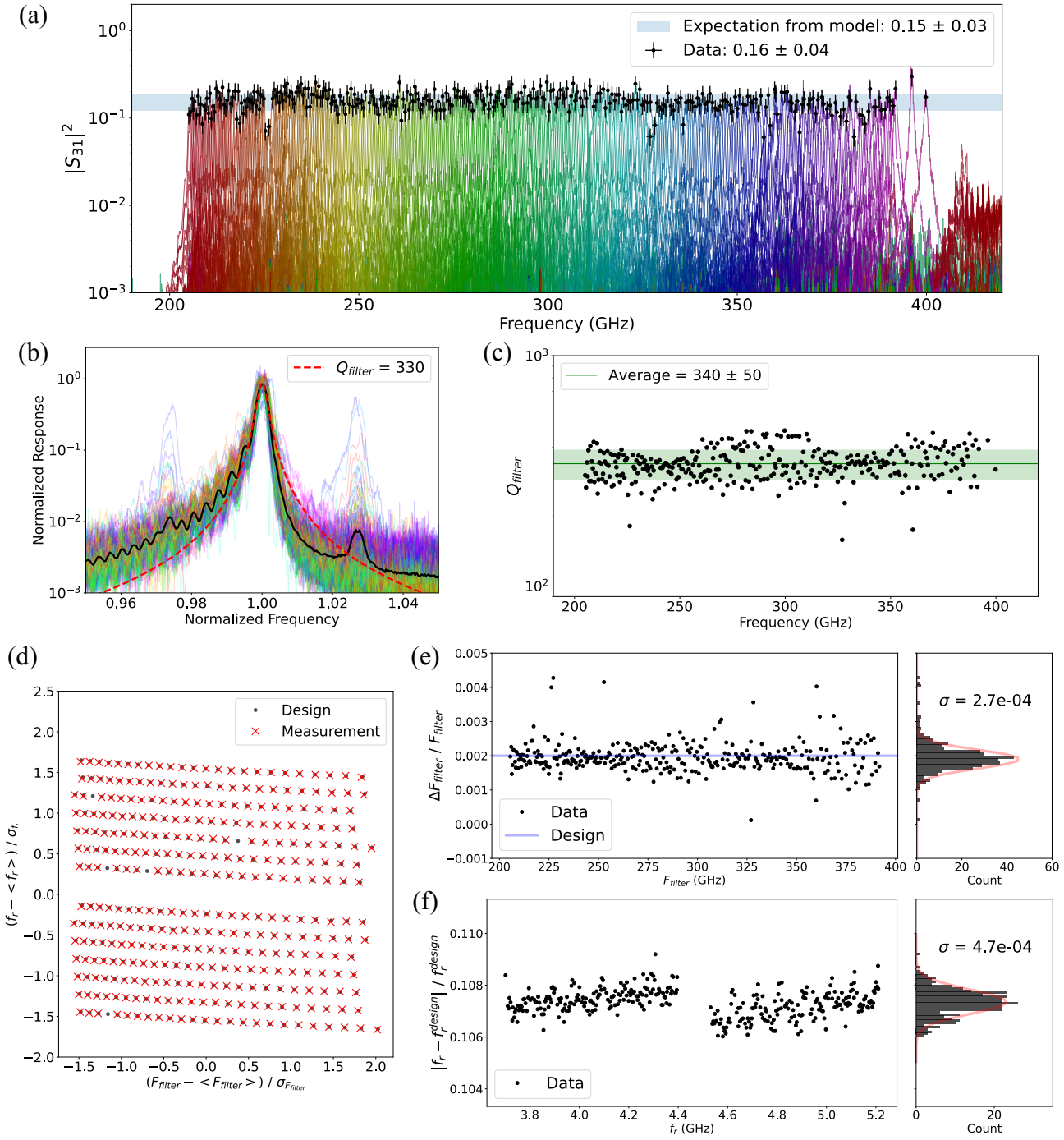


Fig. 5. (a) Measured response of the DESHIMA 2.0 spectral channels, $|S_{31}|^2$. Because they are half-wavelength filters, the second resonances from the lower frequency range (around 200–220 GHz) are also visible above 400 GHz. The black points represent $|S_{31}|^2_{max}$ with error bars, which are a combination of errors from a Lorentzian fit and the design value of $\eta_{wb,bf}$. The blue shaded box shows the expected $|S_{31}|^2_{max}$ from a numerical filterbank model. (b) THz filter responses normalized in the frequency domain (colored curves) and averaged shape (black curve). The dashed red curve shows the result from a Lorentzian fitting to the averaged shape. The obtained Q_{filter} from the fit is ∼330. From the peaks at the normalized frequency of around 0.975 and 1.025 of the averaged shape, we can also estimate a cross-talk level of ∼1% that is mainly caused by the cross talk by neighboring KIDs in the microwave frequency domain. (c) Q_{filter} obtained from the fitting for all THz filters as a function of F_{filter} (black points). The solid green line and shaded area display the averaged Q_{filter} and its standard deviation, respectively. (d) Two-dimensional distribution of the normalized (F_{filter}, f_r). The black points are the design, and the red crosses show the measured data, showing good correspondence between them. (e) Calculated frequency spacing of the THz filters ($\Delta F_{filter}/F_{filter} = (F^{i+1}_{filter} - F^{i}_{filter})/F^{i}_{filter}$) (black points in the left panel) as a function of F_{filter}, and the blue line indicates the design value of 0.02 (= 1/500). The right panel displays the distribution of the frequency spacing with the value of standard deviation (σ) obtained from a Gaussian fit. The result of the fitting is also shown as the red curve in the right panel. (f) Calculated frequency-scattering of KIDs ($|f_r^{measured} - f_r^{design}|/f_r^{design}$) (black points in the left panel) as a function of f_r. The right panel displays the distribution of the frequency-scattering with the value of the standard deviation (σ) obtained from a Gaussian fit. The result of the fitting is also shown as the red curve in the right panel.

where i represents the ith filter, and $x^i_{filter}(F)$ and $x_{wb,bf}(F)$ are the change in KID resonant frequency ($x = \delta f/f_r$) due to the applied CW signal at THz filter i and wideband KID, respectively. The linearity of the detector response was confirmed by repeating the experiment at a lower CW source power, which gave the same result. dx/dP_{abs} is the KID frequency response due to the absorbed power (P_{abs}), and $\eta_{wb,bf}$ is the efficiency of the wideband coupler before the filterbank. We used $\eta_{wb,bf} = -29$ dB, which was obtained by simulations using SONNET. By dividing x_{filter} by $x_{wb,bf}$, all systematic effects before the filterbank entrance were removed, and a pure filter transmission was extracted. $x_{wb,bf}$ is the averaged response of the two wideband coupler KIDs before the filterbank. In this way, the effect of a possible standing wave in the signal line was canceled as the two wideband couplers were placed in the distance of $\lambda_{eff}/4$ of the (sub-)mm wave signal in the signal line, resulting in a 90 degree phase shift and opposite sign for any standing wave. The value of $\eta_{wb,bf} = -29$ dB and the approximation of Eq. (2), which means the equality of the responsivity of all KIDs, were validated experimentally: the detail of how these values were obtained is discussed in Sect. 3.2.

We applied a Lorentzian fit to each filter response, from which we extracted the filter frequency (F_{filter}), the quality factor ($Q_{filter} = Q_i Q_c/(2Q_i + Q_c)$, where Q_c is the coupling from the THz signal line (or KID) to the filter, and Q_i is the internal quality factor of THz filter), and the maximum transmission ($|S_{31}|^2_{max}$) of the THz filter. Using F_{filter}s from the fitting, we normalized the filter responses in the frequency domain and the filter peak values, and the averaged (stacked) shape was calculated (Marting et al., in prep.), which is shown as the black curve in Fig. 5b. The colored curves represent the individual normalized filter responses. The dashed red curve shows the result from a Lorentzian fitting to the averaged shape, and the obtained Q_{filter} from the fit is ∼330. Figure 5c displays the obtained Q_{filter} as a function of F_{filter} from fitting each individual filter response, showing an average value of 340 ± 50. The two results agree with each other, but show smaller Q_{filter} than the design value of 500. Assuming the same coupling Q_c of the filter to the signal line and to the KID, we also estimated a coupling $Q_c \sim 1000$ and an internal $Q_i \sim 1200$ from the dips that emerged in the transmission through the filterbank (S_{21}) calculated by $|S_{21}(F)|^2 = x_{wb,af}(F)/x_{wb,bf}(F)$, where $x_{wb,af}(F)$ represents the averaged response of the two wideband coupler KIDs after the filterbank (the details of this analysis method were described in Pascual Laguna et al. (2021). We conclude that Q_{filter} is lower than designed because Q_i is significantly lower than the value of 6000–10 000 from Buijtendorp et al. (2022).

Figures 5d–f show the quality of the ISS chip. The comparison of the two-dimensional (F_{filter}, f_r) distribution of the measurement with the design is shown in Fig. 5d. The two axes in the figure were normalized by the mean and standard deviation of F_{filter} or f_r to account for frequency shifts in the measured data. The measurement and design values agree well while also highlighting a few missing (F_{filter}, f_r) pairs in the measurement dataset. As a result, 334 out of 339 THz filters were identified, which means a yield of more than 98%. Figure 5e displays the spacing of the THz filter frequencies, $\Delta F_{filter}/F_{filter} = (F^{i+1}_{filter} - F^i_{filter})/F^i_{filter}$, from the measurement. We obtained a nearly constant value of $\Delta F_{filter}/F_{filter} = 0.02$ with a standard deviation of 2.7×10^{-4}, which is much lower than the filter spacing. The residual slope on the line indicates a slow spatially varying systematic variation in the parameter determining the filter frequencies. The frequency spacing of the filterbank can be expressed as a quality factor, Q_{space}, that was calculated as $Q_{space} = F_{filter}/\Delta F_{filter} = 500$. It agrees well with the design value. We also evaluated the frequency scattering of KID, as shown in Fig. 5f, by calculating the absolute deviation between the measured and designed frequencies. We computed $|f_r^{measured} - f_r^{design}|/f_r^{design}$, yielding a $\sigma = 4.7 \times 10^{-4}$ by a Gaussian fitting. This is interestingly very similar to the filter frequency scatter. This result was achieved through our two-step patterning process for the Al layer without employing trimming techniques (Liu et al. 2017; Shu et al. 2018), demonstrating the quality of the fabrication process (Thoen et al. 2022).

The averaged $|S_{31}|^2_{max}$ from measurement was 0.16 ± 0.04, as indicated in the legend of Fig. 5a. This value is lower than the theoretical maximum coupling of a half-wavelength filter, which is 0.5. Three factors contributed to this discrepancy. The first effect was the low Q_i of the filters because of dielectric loss. This caused part of the power to be lost in the dielectric and more power to pass the filter to the next channel. This reduced the peak transmission value from 0.5 to 0.24 (Pascual Laguna et al. 2021). The second cause was an internal oversampling. The difference between $Q_{filter} = 340$ and $Q_{space} = 500$ led to power being partially shared among neighboring filter channels. This resulted in lowering the peak value from 0.24 to 0.17, which was estimated by a numerial filterbank model (Marting et al. 2024). The third effect was the variation in the filter frequency $\Delta F_{filter}/F_{filter}$. This further increased the effect of sharing power among neighboring channels. By including the measured variation (2.7×10^{-4}) together with the oversampling in the numerical model, we obtained an expected peak value of 0.15 ± 0.03, which matches the measurement well.

3.2. Instrument sensitivity

We evaluated the instrument sensitivity with two measurements: the KIDs response measurement using two blackbody radiators, one at room temperature ($T_{room} = 300$ K) and the other at the temperature of liquid nitrogen ($T_{cold} = 77$ K), and a noise measurement. During the response measurement, we placed two temperature loads at positions 1 and 2, indicated in Fig. 4, along the optical path of the chopper. We then measured the response of KIDs in the time domain by switching between these positions in 10 Hz through the rotational motion of the chopper. In the noise measurement, 300 s long time domain data were taken with a sampling speed of ∼1.3 kHz by fixing the chopper to the path where T_{cold} was placed. The noise power spectrum density (PSD) was then calculated from the time stream data to obtain the KID photon noise level and knee frequency of its $1/f$ noise. From the measured KID response and noise PSD, we evaluated the noise equivalent power (NEP) and optical efficiency of the whole instrument.

Figure 6a illustrates an example of how the KID response, $x = \delta f/f_r$, was extracted from the optical response measurement. In this example, T_{cold} and T_{room} were placed at position 1 and position 2, respectively. The top panel shows data from the diode sensor inside the chopper. We took the diode data with a sampling frequency around 800 Hz, which is lower than the KID readout speed of ∼1.3 kHz. To address this mismatch, we interpolated the points by the time stamp of the KID readout, so that the diode data in the figure include intermediate states. As an example, the bottom panel displays the filter KID response at $F_{filter} = 299$ GHz, showing good synchronization with the diode data. The response for each KID was evaluated by taking the difference between two temperature loads. With a sampling rate of ∼1.3 kHz and chopping frequency of 10 Hz, we observed

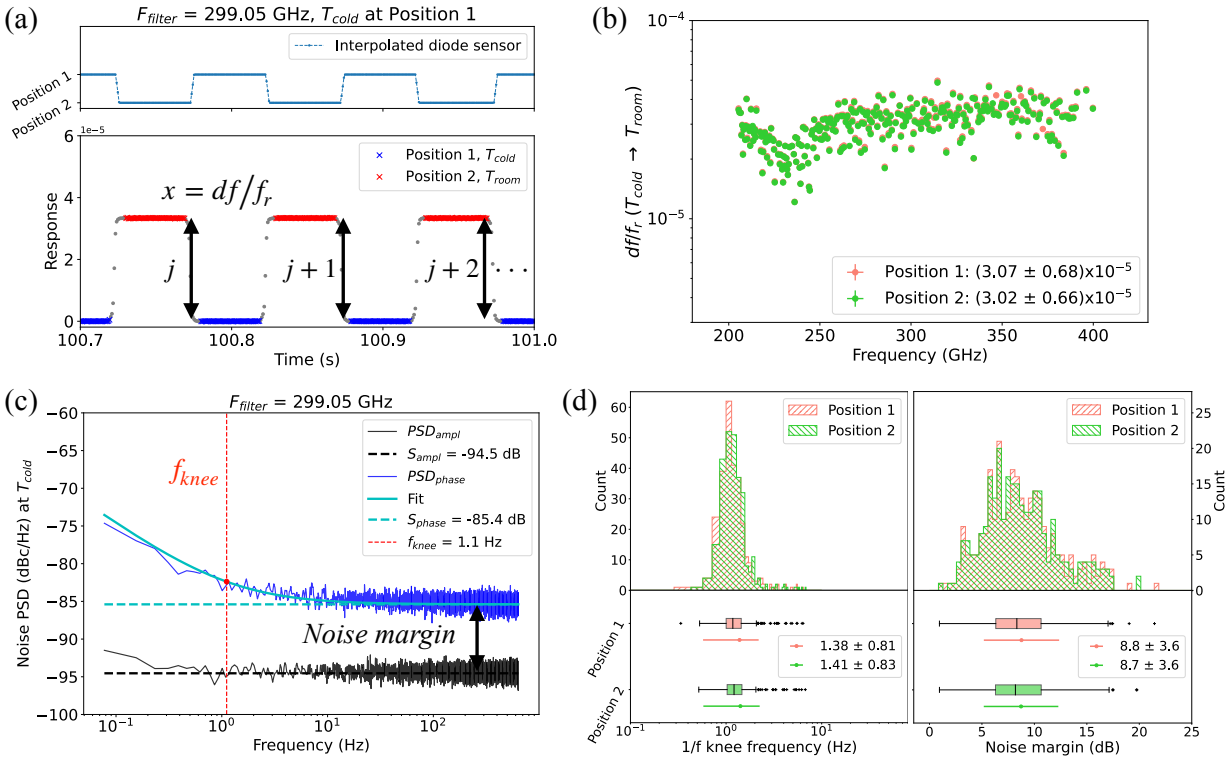


Fig. 6. (a) Time domain data (example) of the F_{filter} = 299.05 GHz filter KID from the response measurement with the chopper, placing T_{cold} at position 1. The top panel shows the interpolated data from the diode sensor by the timestamp of the KID readout. The bottom panel displays the KID response: The gray points show the KID response, and the blue and red crosses represent the data points tagged as position 1 (T_{cold}) and position 2 (T_{room}) by the chopper diode data, respectively. (b) x_{meas} obtained as a function of F_{filter} with the averaged value and standard deviation in the legend. The pink and green points correspond to the data when T_{cold} was placed at position 1 and position 2, respectively. (c) Noise PSD (example) of the F_{filter} = 299.05 GHz filter KID from the noise measurement. The blue and black curves represents the measured phase and amplitude noise PSD of the KID, respectively. The fit result to the phase PSD is shown as a cyan line, and the dashed lines represent the noise floor of the phase (cyan) and amplitude (black) PSDs. The vertical dashed red line represents f_{knee} of the phase noise PSD. (d) Distribution of f_{knee} (top left), with its box plot, averaged value, and standard deviation in the bottom left panel. The pink and green colors correspond to the data when T_{cold} is placed at position 1 and position 2, respectively. The top right panel displays the distribution of noise margin ($S_{phase} - S_{ampl}$ in dB unit), with its box plot, averaged value, and standard deviation in the bottom right panel. The color-code is same as in the left panel.

approximately 130 points in one cycle. However, due to transitions between the two chopper positions, about 24 points were discarded, which were determined using the diode data. This resulted in a data loss of less than 20% overall, meaning an effective chopping efficiency of ~80%. To account for slow drifts (1/f noise), we calculated x values at each cycle (denoted as j, $j+1$, $j+2$... in the figure) and averaged them over the entire dataset: we write the averaged value as x_{meas} hereafter. Figure 6b shows the measured x_{meas} as a function of F_{filter}. The responses were almost identical when T_{cold} was placed in position 1 or position 2. A small dip around 230–240 GHz was due to the transmittance of the IR blocking filter stack shown in Fig. 2c.

Figure 6c displays the measured noise PSD of the F_{filter} = 299 GHz filter KID. To characterize the noise properties of all KIDs, we fitted the noise PSDs with a function of the form $a_0 + a_1/f$, where a_0, a_1 are fitting parameters, and f represents the frequency in the readout domain. This analysis allowed us to determine the knee frequencies ($f_{knee} \equiv a_1/a_0$) associated with 1/f noise and the white-noise levels (S_{ampl} or $S_{phase} \equiv a_0$). The $1/f$ noise was mainly caused by TLS noise of the KIDs themselves, so that we only evaluated f_{knee} in the phase noise. The distribution of f_{knee} from all KIDs is plotted in the left panel of Fig. 6d, showing an averaged f_{knee} of about 1.4 Hz, which was well below the chopping frequency of 10 Hz, without any significant discrepancy between positions 1 and 2. Furthermore, since S_{ampl} was at the same level as the readout electronics noise measured by the blind tones, the white phase noise (S_{phase}) at $f > 10$ Hz (see Fig 6c) is direct evidence of the photon-noise-limited performance (Janssen et al. 2013) because white noise is either due to quasi-particle fluctuations caused by photon fluctuations under optical loading, as is the case here, or to the readout system. To quantify this, we calculated a noise margin for each KID, defined as the difference between the S_{phase} and S_{ampl} values in dB units (i.e., $S_{phase} - S_{ampl}$, as indicated in Fig. 6c). The distribution of the noise margin is plotted in the right panel of Fig. 6d. The averaged noise margin across all KIDs was about 8.8 dB, which ensured the photon-noise-limited sensitivity of the DESHIMA ISS system. A lower $1/f$ noise knee and higher photon noise level can be created by reducing the aluminum volume, but this comes as at the cost of the KID dynamic range, which makes observations at varying sky opacities more cumbersome.

Using the measured KIDs responses and the noise PSDs, we determined NEP at the loading temperature T_{cold} experimentally by

$$NEP^i_{exp} = \sqrt{S^i_x} \times \left(\frac{dx^i}{dP^i_{rad}}\bigg|_{T_{cold}} \right)^{-1}. \quad (3)$$

Here, S_x represents the frequency noise, which can be derived from S_{phase} using the relation of $S_x = S_{phase}/4Q_r$, and dx/dP_{rad}

is the KID responsivity, representing how strongly the KID responses to changes in the loading power (P_{rad}). The subscript T_{cold} indicates that we used a readout tone at the KID resonant frequency at the lowest load temperature.

P_{rad} can be defined at any reference plane. In this paper, we defined P_{rad} as the loading power in front of the Si lens. Then, P_{rad} was calculated by

$$P^i_{rad}(T_{load}) = \int dF\ \frac{1}{2} B(T_{load}, F)\lambda^2 T^i(F), \tag{4}$$

$$T^i(F) = t_{IR}(F) \times \left(x^{i,\,norm}_{filter}(F)\ /\ x^{norm}_{wb,bf}(F)\right), \tag{5}$$

where $B(T, F)$ is the radiator irradiance, the factor 1/2 shows the polarization efficiency, and $\lambda^2 = (c/F)^2 = A\Omega$ is the total throughput, both representing a single-polarization single-mode detector. $t_{IR}(F)$ is the total transmission of IR-blocking filters shown in Fig. 2c, and $x^{norm}(F) = x(F)\ /\ \max\{x(F)\}$ represents the normalized filter response, where $x_{filter}(F)$ and $x_{wb,bf}(F)$ are taken from the THz frequency response presented in Sect. 3.1. In this way, we extracted the optical efficiency with respect to the Si lens, denoted as η_{opt}, by equating NEP_{exp} to the theoretical photon-noise-limited NEP, as discussed below. Hence, η_{opt} represents the combined efficiency of the leaky-wave antenna and a THz filter, and the absorbed power by the KID (P_{abs}) can be expressed as $P_{abs} = \eta_{opt} P_{rad}$. For wideband KIDs, the factor $x^{i,\,norm}_{filter}(F)/x^{norm}_{wb,bf}(F)$ in Eq. (5) was replaced by the normalized frequency response from simulations using SONNET. For dark KIDs, the factor was replaced by unity.

To calculate the KID responsivity (dx/dP_{rad}), nonlinear effects need to be considered, especially when the KID response is measured using two very different temperature loads, such as T_{cold} and T_{room} (Takekoshi et al. 2020). Since the KID response scales as $\sqrt{P_{abs}} \propto \sqrt{P_{rad}}$ (de Visser et al. 2014), x can be expressed as $x = k\sqrt{P_{rad}}$ with a proportional constant k. Here, x is the KID frequency shift with respect to zero loading power, that is, $x = (f - f^0_r)/f^0_r$ with f^0_r representing the resonance frequency at zero loading power. Therefore, in our measurement, $x_{meas} = (f_r^{T_{room}} - f_r^{T_{cold}})/f_r^{T_{cold}}$ can be related to k as

$$x^i_{meas} \times f_r^{i,T_{cold}}/f_r^{i,0} = k^i\left(\sqrt{P^i_{rad}(T_{room})} - \sqrt{P^i_{rad}(T_{cold})}\right), \tag{6}$$

so that the KID responsivity was calculated by

$$\left.\frac{dx^i}{dP^i_{rad}}\right|_{T_{load}} = \frac{k^i}{2\sqrt{P^i_{rad}(T_{load})}}$$

$$= \frac{1}{2\sqrt{P^i_{rad}(T_{load})}} \cdot \frac{x^i_{meas} \times (f_r^{i,T_{cold}}/f_r^{i,0})}{\sqrt{P^i_{rad}(T_{room})} - \sqrt{P^i_{rad}(T_{cold})}} \tag{7}$$

$$\sim \frac{1}{2\sqrt{P^i_{rad}(T_{load})}} \cdot \frac{x^i_{meas}}{\sqrt{P^i_{rad}(T_{room})} - \sqrt{P^i_{rad}(T_{cold})}}. \tag{8}$$

We approximated f^0_r by the KID resonance frequency measured in the dark condition by closing the optical window (denoted as f^{dark}_r). The difference between f^{dark}_r and $f_r^{T_{cold}}$ was measured to be smaller than 1 MHz, which justified the approximation of $f_r^{T_{cold}}/f^0_r \sim 1$ within the 0.1% uncertainty because KID resonance frequencies were in the range of 4–6 GHz.

The optical efficiency with respect to the Si lens, η_{opt}, was then calculated with the assumption of the photon-noise-limited sensitivity. By equating the calculated NEP_{exp} to the theoretical optical NEP of photon-noise-limited KIDs (Ferrari et al. 2018), we obtained η_{opt} as

$$\eta^i_{opt} = \frac{2P^i_{rad}hF^i_{filter} + 4P^i_{rad}\Delta/\eta_{pb}}{(NEP^i_{exp})^2 - 2(P^i_{rad})^2/\Delta F^i}, \tag{9}$$

where h is the Planck constant, Δ is the superconducting gap energy of Al film, $\eta_{pb} \sim 0.4$ is the pair-breaking efficiency (Guruswamy et al. 2014), and ΔF^i represents equivalent bandwidth calculated by $\Delta F^i = \int dF\ T^i(F)$. As mentioned above, η_{opt} is a product of a THz filter efficiency, η_{filter}, and the leaky-wave antenna efficiency, η_{leaky}, that is, $\eta^i_{opt} = \eta^i_{filter} \times \eta_{leaky}$, where η_{leaky} further breaks down into spill-over from the antenna beam on the lens surface, the fraction of the power radiated to the front side of the lens, the fraction of the power coupled to the CPW signal line, the reflection at the lens surface, and spill-over from the cold mirrors. In total, η_{leaky} is ~0.7 by the design (Dabironezare et al., in prep.).

The instrument efficiency (η_{inst}) and NEP (NEP_{inst}), which we defined in this paper as the efficiency and NEP with respect to the entrance of the instrument (MP 2 in Fig. 4; i.e.. the entrance of the chopper), were calculated by the following the equation

$$\eta^i_{inst} = \eta^i_{opt} \times t_{IR}(F^i_{filter})$$

$$= \eta^i_{filter} \times \eta_{leaky} \times t_{IR}(F^i_{filter}), \tag{10}$$

$$NEP^i_{inst} = NEP^i_{exp} \times \left(t_{IR}(F^i_{filter})\right)^{-1}. \tag{11}$$

We assumed that the loss in the warm optics chain, such as spill-over loss from the warm mirrors or the chopper, was negligible. In order to check this assumption, we also performed the optical sensitivity measurement at MP 1 (in front of the cryostat window; see Fig. 4), but without the chopper, by exchanging T_{room} and T_{cold} alternately on a timescale of a few dozen seconds. The obtained η_{opt} values were consistent.

Figures 7a and b display η_{inst} and NEP_{inst} we obtained as a function of F_{filter}, respectively. Both quantities are distributed quite uniformly over the frequency band. The averaged η_{inst} was ~8%, and the averaged NEP_{inst} was $\sim 1.3 \times 10^{-16}$ W/$\sqrt{Hz}$, without any significant difference between positions 1 and 2. In Fig. 7a we also plot η_{inst} calculated using $|S_{31}|^2_{max}$ in Fig. 5a, which was an equivalent quantity to η_{filter}, with black points as reference. The consistency between two separate results (from steps 1 and 4 in Sect. 2.3) increases the reliability of the obtained results.

Along with the instrument efficiency, we also evaluated the efficiency of wideband coupler KIDs and dark KIDs, as shown in Fig. 8. In the plot, we removed the contribution from η_{leaky} by calculating the ratio η_{opt}/η_{leaky} to evaluate the wideband coupler coupling and stray-light effects alone. As a result, the averaged coupling strength of the wideband coupler KIDs before ($\eta_{wb,bf}$) and after ($\eta_{wb,af}$) the filterbank were measured to be -30 ± 1 dB and -36 ± 1 dB, respectively. The results show that $\eta_{wb,bf}$ was consistent with the design of -29 ± 1 dB, while $\eta_{wb,af}$ was 6–7 dB lower, indicating that the power was reduced by a factor of 4 to 5 due to power absorbed in the filterbank. The averaged coupling strength of the dark KIDs was -46 ± 2 dB, which was about -38 dB lower than η_{filter} (average ~0.16 = -8 dB), showing that the stray-light effect on the KID detectors was very small.

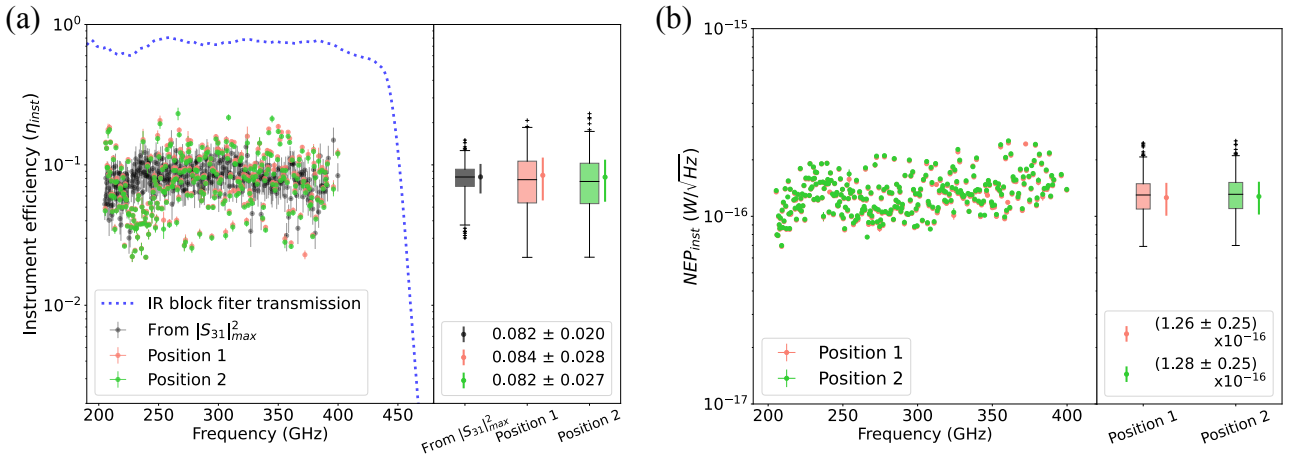


Fig. 7. (a) Instrument efficiency (η_{inst}; left panel) as a function of F_{filter}, with its box plot, averaged value, and standard deviation in the right panel. Pink and green correspond to the data when T_{cold} was placedat position 1 and position 2, respectively. The error bars of the pink and green points were a combination of the statistical uncertainties from the response calculation and fitting error of the noise PSD. The black points show η_{inst}, calculated using $|S_{31}|^2_{max}$ in Fig. 5a. The error bars were from uncertainties of $|S_{31}|^2_{max}$. The dotted blue curve represents the total transmission of the IR-blocking filters and Si window ($t_{IR}(F)$), as shown in Fig. 2c. (b) Instrument optical NEP (NEP_{inst}; left panel) as a function of F_{filter}, with its box plot, averaged value, and standard deviation in the right panel. Pink and green correspond to the data when T_{cold} was placed at position 1 and position 2, respectively.

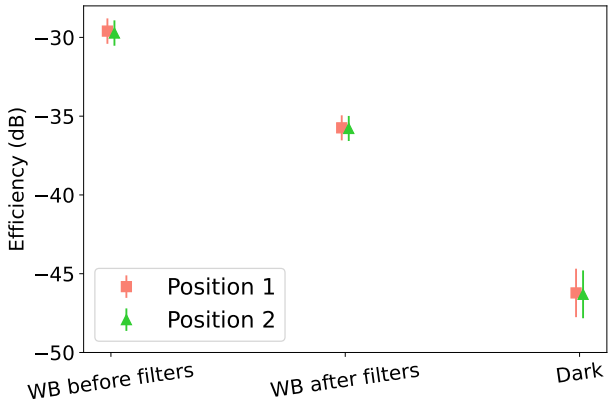


Fig. 8. Measured efficiencies of the wideband couplers before (left row) and after (middle row) the filterbank, and the dark KID (right row). The numbers of KIDs of the wideband couplers before, after, and dark are 2, 2, and 4, respectively, but we plot averaged values here. The error bars are a combination of the variation when averaging in each group, statistical uncertainties from the response calculation, and fitting error of the noise PSD. The pink squares and green triangles correspond to the data when T_{cold} was placed at position 1 and position 2, respectively.

3.3. Beam characteristics

We measured the phase and amplitude (PA) beam patterns of the instrument at MP 2 in Fig. 4, following a quasi-heterodyne measurement technique (Davis et al. 2019; Yates et al. 2020), which allowed us to obtain the PA beam patterns using any KID in the ISS as detector. The PA information was essential to investigate the misalignment of the instrument and also to propagate the measured beam pattern numerically through the telescope reflectors to estimate the expected performance of the instrument at the telescope. The experimental procedure was similar to that of Endo et al. (2019a), but we extended the PA measurement to a so-called harmonic phase and amplitude (HPA) measurement. This uses two broadband mixers (Paveliev et al. 2012) to generate overtones at integer multiples of the pump signal of $f_{synth} \sim 9.76548$ GHz, which were fed from two synthesizers connected to the mixers. The frequency of the generated radiation was $n \times f_{synth}$, and the integer range of $n = 21$–40 corresponded to the frequency range of the DESHIMA 2.0. The two synthesizers had a small frequency difference of $\Delta f \sim 12$ Hz, resulting in a THz frequency offset of $\Delta F = n \times \Delta f$ that modulated the detector response in the time domain. Δf was chosen in such a way that the ΔF with $n = 40$ was well within the bandwidth of the detectors and readout system with a sampling speed of ∼1.3 kHz. In this way, the KIDs responses at the modulation frequency of ΔF in the readout domain were correlated to the incoming source signal of the frequency of $n \times f_{synth}$. As KIDs are not phase-sensitive detectors, the modulation of Δf was separately measured by adding it to all the readout tones in the multiplexing readout: the phase of this modulation was used as a phase reference. The complex field parameters (phase and amplitude of the source signal) were then obtained by the values at the frequency of ΔFs of a complex fast Fourier transform (FFT) of the time-domain data by normalizing the FFT phase by the phase reference. While one mixer is fixed, the other mixer can be moved in a scanning plane, which allowed us to map PA beam patterns as a function of the scanning position across the harmonic range of THz frequencies simultaneously. More details of the experiment are given in Moerman et al. (2024). As the origin of the harmonic frequencies is a well-calibrated signal from the synthesizers, we also used these data for the absolute frequency calibration of the THz filter frequencies, which is discussed in Sect. 3.4.

We used the measured PA beam patterns to estimate the expected performance of the instrument at the telescope by propagating them through a model of ASTE using PyPO. Our study was limited to 20 filters, whose frequencies matched the harmonic frequencies in the HPA measurement, that is, $n \times f_{synth}$, with integer values ranging from $n = 21$ to 40. These results are shown in Fig. 9.

We first evaluated the antenna efficiencies, consisting of the spillover efficiency on the sub-reflector (η_{so}^{sub}), the taper efficiency in the aperture of the main reflector (η_t), and the aperture efficiency $\eta_{ap} = \eta_{so}^{sub} \times \eta_t$. Figure 9a displays the obtained η_{ap} for

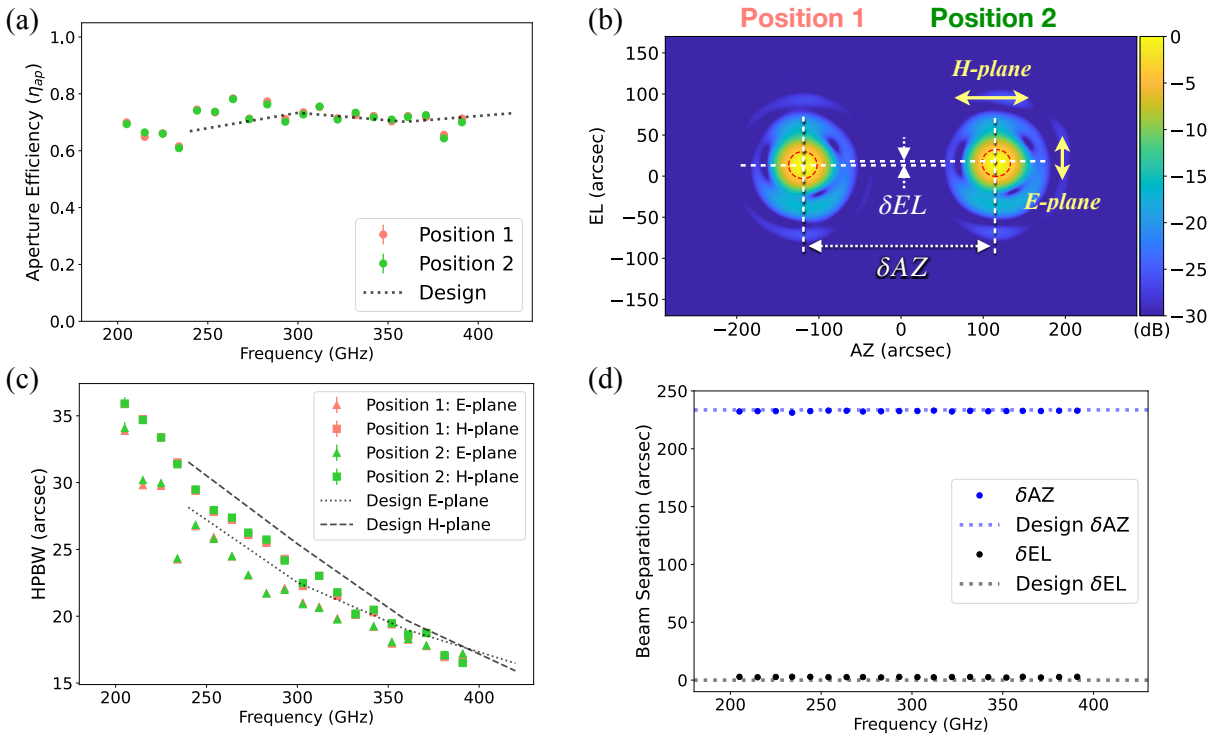


Fig. 9. Expected performance of the DESHIMA 2.0 instrument on the ASTE telescope based upon the laboratory PA beam pattern measurements. (a) Obtained aperture efficiency (η_{ap}) as a function of filter frequency (20 filters matched to the harmonic frequencies). Pink and green correspond to the beam pattern data measured at position 1 and position 2, respectively. The dotted black curve represents the design specification. (b) Telescope far-field beam patterns of the 205 GHz filter in the two paths of positions 1 and 2. The dashed red lines plot 3 dB contours from the results of the two-dimensional Gaussian fittings. The definitions of the E and H planes are indicated by yellow arrows: the E-plane is aligned along the semiminor axis of the far-field main beam, and the H-plane is parallel to the semimajor axis. The definitions of the beam separation (δAZ, δEL) are also illustrated in the figure. (c) Obtained HPBW in the E-plane (triangle points) and H-plane (square points) as a function of the filter frequency. Pink and green correspond to the beam pattern data measured at position 1 and position 2, respectively. The dotted and dashed black curves represent the design specification of the E- and H-plane, respectively. (d) Beam separation as a function of filter frequency. The blue and black points are the evaluated δAZ and δEL, respectively, with the design value plotted as dotted lines.

the two beam positions after the chopper. We found an average value of ~0.7, which agrees well with the design value indicated by the dashed line in the figure, while also showing no significant difference between positions 1 and 2. We also obtained η_{so}^{sub}~0.9, which is slightly lower than the designed value of 0.95, and η_t~0.8, which is slightly higher than the design value of 0.75. The combined effect is a slight increase in the edge illumination on the sub-reflector compared to the design. This also results in a higher illumination at the outer section of the main reflector. Consequently, while the increased illumination at the edge does not significantly impact the instrument performance (as evidenced by the good agreement between the measured and designed η_{ap} values), it results in a decrease in beam size in the far field, which was consistent with smaller half-power beam widths (HPBWs) than originally specified, as displayed in Fig. 9c. Here, η_t was calculated in the aperture plane perpendicular to the telescope pointing, which was in the direction of maximum directivity and off from the broadside in the azimuthal direction due to the two separated paths (positions 1 and 2) in the sky chopper (for more details of the definition and calculation of these efficiencies, see Appendix of Moerman et al. 2024). We also note that η_{ap} here does not contain the surface error of the ASTE telescope. The DESHIMA 2.0 instrument at ASTE, including the surface error, was optically verified, and the details are described in Moerman et al. (2025).

An example of the expected telescope far-field beam pattern of the 205 GHz filter (corresponding to the 21 st harmonic frequency) is displayed in Fig. 9b. As the coordinates of the measurement plane (MP 2) were properly implemented in the telescope model through the alignment process, the far-field beam patterns from positions 1 and 2 showed an offset from the telescope broadside ($AZ = EL = 0$), as expected. To extract the beam characteristics such as pointing (beam center) and half-power beam widths (HPBW), we fitted the far-field beam patterns to a two-dimensional Gaussian function. Figure 9c displays the obtained HPBWs in the E- and H-plane as a function of filter frequency, again showing no significant discrepancy between positions 1 and 2. The definition of the E and H planes is illustrated in Fig. 9b. The HPBWs were slightly smaller than the design values at all measured frequencies. As discussed above, we attributed this discrepancy to a higher edge illumination on the sub-reflector, which might also explain the lower η_{so}^{sub} and higher η_t. Furthermore, using the obtained beam centers from the fitting, we also estimated the beam separation between the far-field beam patterns of positions 1 and 2. We calculated δAZ and δEL. This definition is also illustrated in Fig. 9b and is plotted in Fig. 9d as a function of filter frequency. The averaged δAZ and δEL were 232.6 ± 1.5 and 2.6 ± 1.9 arcsec, respectively, which were consistent with the design specification of $\delta AZ = 234$ and $\delta EL = 0$ arcsec.

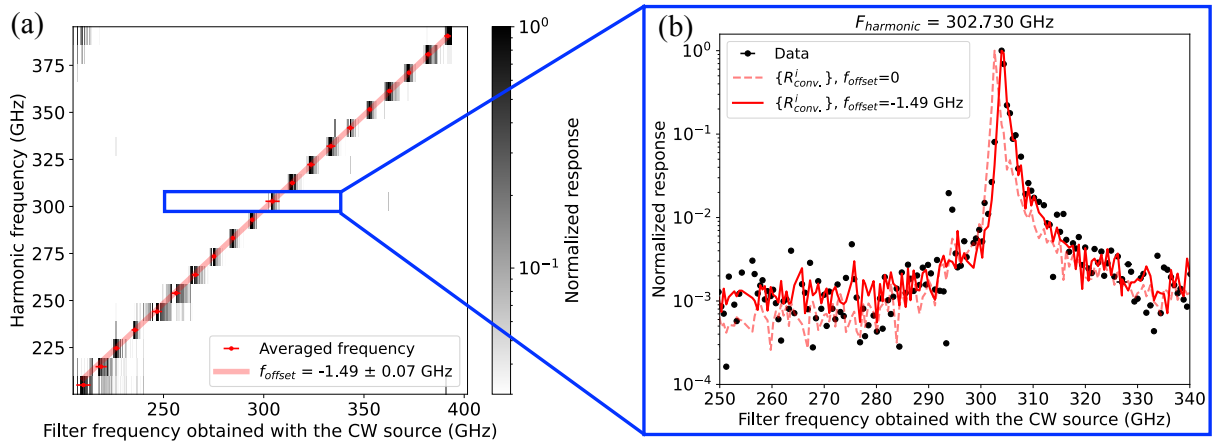


Fig. 10. (a) Two-dimensional plot of the normalized KIDs responses obtained from the HPA beam pattern measurement. The vertical axis shows the harmonic frequency, and the horizontal axis presents the filter frequency measured with the CW source. Due to the second resonances of the lower frequency filters (the filter peaks around 200–220 GHz), they also respond to signals from high harmonic frequencies (black points around the top left corner of the figure). The red points represent the weighted average of the filter frequencies by the KIDs responses, and the red curve shows the result from a linear fit. The blue box in the figure indicates the plotted data in panel (b). (b) Comparison of the measured data (black points) and the convolved response of $\{R^i_{conv.}\}$ / max$\{R^i_{conv.}\}$ for the harmonic frequency of 302.730 GHz. The dashed and solid red curves are convolved responses with $f_{offset} = 0$ and -1.49 GHz, respectively.

3.4. Absolute frequency calibration

Because of the frequency uncertainty of 2 GHz from the CW source used in the experiment in step 1, we carried out an absolute frequency calibration of the filters using the data from the experiment in step 3, in which the harmonic frequencies were generated by well-calibrated signals from a synthesizer. Figure 10a illustrates this method. The vertical axis shows the frequency generated by means of the synthesizer and harmonic mixers, and the horizontal axis presents thefilter frequency measured with the CW source. The grayscale points in the figure show the KIDs responses normalized to the maximum response at each frequency generated by the harmonic mixer, and the red points represent the weighted average of the filter frequencies by the KIDs responses. We fitted the red points by a linear function with the intercept as a fitting parameter (denoted as f_{offset}), while fixing the slope to unity. As a result, we obtained $f_{offset} = -1.49 \pm 0.07$ GHz, which was consistent with the 2 GHz accuracy of the CW source, demonstrating an improvement of the absolute frequency calibration of the filterbank with the data from the HPA beam pattern measurement. When we also included the slope of the line as a fit parameter, the result did not change, indicating that we can use f_{offset} as the only parameter to correct the DESHIMA 2.0 absolute filter frequencies.

Figure 10b shows how the obtained f_{offset} improved the match between the measured data (black points, normalized to their maximum) and the convolved responses (red curves). The convolved responses were calculated by the following formula:

$$R^i_{conv.} = \int dF\, T^i(F + f_{offset})\, \delta(F - F_{harmonic}) \quad (12)$$

$$= T^i(F_{harmonic} + f_{offset}), \quad (13)$$

where i denotes the ith filter, $T^i(F)$ is the transmission of filter i (same as in Eq. (5)), $\delta(F)$ represents the Dirac delta function, and $F_{harmonic}$ is the harmonic frequency from the HPA beam pattern measurement. We used the delta function in the convolution because the tone bandwidth from the harmonic mixer was much narrower than Q_{filter}, resulting in $R^i_{conv.}$ equal to the interpolated ith filter transmission value at $F = F_{harmonic} + f_{offset}$. The red curves in the figure show two sets of $\{R^i_{conv.}\}$ of all ith filters at $F_{harmonic} = 302.730$ GHz with $f_{offset} = -1.49$ GHz (solid red curve) and $f_{offset} = 0$ (dashed red curve; both normalized by the maximum value in each set). The convolved response with $f_{offset} = -1.49$ GHz agrees better with the measured data (black points), especially around the peak.

4. Conclusions

We presented extensive characterizations of the DESHIMA 2.0 instrument in laboratory measurements. The measured frequency coverage was 200–400 GHz with a mean Q_{filter} of 340 ± 50, lower than the design value of $Q_{filter} = 500$, which is caused by a low MS filter $Q_i \sim 1200$ and an instrument efficiency of ∼8%, indicating a four times wider band coverage and a four times higher coupling efficiency than DESHIMA 1.0. The filter separation was found to be $Q_{space} = F_{filter}/\Delta F_{filter} = 500$, exactly as designed, with a very low scatter given by $\sigma_{\Delta F_{filter}/F_{filter}} = 2.7 \times 10^{-4}$, showing excellent control of the fabrication process. We identified 334 out of 339 THz filters, which means a yield rate of more than 98%. The KID phase noise showed the photon-noise-limited sensitivity with a mean f_{knee} of 1.4 Hz, which is well below 10 Hz of the chopping speed of the sky-position chopper. The data loss caused by the chopper was lower than 20%, and the telescope far-field beam patterns through the chopper matched the calculated field distributions exactly, importantly showing no truncation by the chopper construction. Moreover, the beam separation for the two chopper positions matched the design well. The estimated aperture efficiency was found to agree well with the designed value of approximately 70%. We also demonstrated the validity of a new method of absolute frequency calibration using the data from the HPA beam pattern measurement.

To improve the instrument efficiency in future developments, a few potential strategies might be explored: (i) increasing Q_i of the dielectric by using a different material (Defrance et al. 2025), (ii) matching Q_{filter} and Q_{space} from the current $Q_{space} >$

Q_{filter}, which causes signal leakage to neighboring filters, and (iii) using directional filters, which offer significantly higher in-band transmission (theoretical maximum in-band coupling of unity (Marting et al. 2024), compared to ~0.5 for our current filter design). These developments will increase the instrument efficiency to be comparable with heterodyne receivers. Together with the scalability to IFUs with $\gtrsim$100 spatial pixels, the ISS technology will lead to unique astronomical instruments that complement the existing large-scale interferometers.

Acknowledgements. This work was supported by the European Union (ERC Consolidator Grant Nos. 648135 MOSAIC and 101043486 TIFUUN). Views and opinions expressed are however those of the authors only and do not necessarily reflect those of the European Union or the European Research Council Executive Agency. Neither the European Union nor the granting authority can be held responsible for them. This research was also supported by the Netherlands Organization for Scientific Research NWO (Vidi Grant No. 639.042.423, NWO Medium Investment Grant No. 614.061.611 DESHIMA, and Open XS grant OCENW.XS22.4.146), A.P.L. was supported by the Juan de la Cierva grant JDC2023-051842-I funded by the Spanish MCIN/AEI/10.13039/501100011033. M.R. is supported by the NWO Veni project "Under the lens" (VI.Veni.202.225). T.T. was supported by the MEXT Leading Initiative for Excellent Young Researchers (Grant No. JPMXS0320200188). This study was also supported by the JSPS KAKENHI (Grant Nos. JP22H04939, JP23K20035, JP24H00004, and JP24H01808).

References

Baselmans, J. J. A., Bueno, J., Yates, S. J. C., et al. 2017, A&A, 601, A89
Baselmans, J. J. A., Yates, S., Diener, P., & de Visser, P. J. 2012, J. Low Temp. Phys., 167, 360
Baselmans, J. J. A., Facchin, F., Pascual Laguna, A., et al. 2022, A&A, 665, A17
Bisigello, L., Yates, S. J. C., Murugesan, V., Baselmans, J. J. A., & Baryshev, A. M. 2016, J. Low Temp. Phys., 184, 161
Buijtendorp, B. T., Vollebregt, S., Karatsu, K., et al. 2022, Phys. Rev. Appl., 18, 064003
Buijtendorp, B. T., Endo, A., Jellema, W., et al. 2025, Phys. Rev. Appl., 23, 014035
Carilli, C. L., & Wang, R. 2006, AJ, 131, 2763
Davis, K. K., Yates, S. J. C., Jellema, W., et al. 2019, IEEE Trans. Terahertz Sci. Technol., 9, 67
Day, P. K., LeDuc, H. G., Mazin, B. A., Vayonakis, A., & Zmuidzinas, J. 2003, Nature, 425, 817
de Visser, P. J., Baselmans, J. J. A., Bueno, J., Llombart, N., & Klapwijk, T. M. 2014, Nat. Commun., 5, 3130
Defrance, F., Beyer, A. D., Wheeler, J., Sayers, J., & Golwala, S. R. 2025, Appl. Phys. Lett., 126, 122904
Dragone, C. 1978, Bell Labs Tech. J., 57, 2663
Endo, A., Karatsu, K., Pascual Laguna, A., et al. 2019a, J. Astron. Telesc. Instrum. Syst., 5, 035004
Endo, A., Karatsu, K., Tamura, Y., et al. 2019b, Nat. Astron., 3, 989
Ferrari, L., Yurduseven, O., Llombart, N., et al. 2018, IEEE Trans. Terahertz Sci. Technol., 8, 127
Gao, J. 2008, PhD thesis, California Institute of Technology
Gao, J., Daal, M., Vayonakis, A., et al. 2008, Appl. Phys. Lett., 92, 152505
Guruswamy, T., Goldie, D. J., & Withington, S. 2014, Supercond. Sci. Technol., 27, 055012
Hähnle, S., Yurduseven, O., van Berkel, S. L., et al. 2020, IEEE Trans. Antennas Propag., 68, 5675
Janssen, R. M. J., Baselmans, J. J. A., Endo, A., et al. 2013, Appl. Phys. Lett., 103, 203503
Karkare, K. S., Barry, P. S., Bradford, C. M., et al. 2020, J. Low Temp. Phys., 199, 849
Karkare, K. S., Anderson, A. J., Barry, P. S., et al. 2022, J. Low Temp. Phys., 209, 758
Klaassen, T. O., Diez, M. C., Blok, J. H., et al. 2001, in Proc. of the 12th International Symposium on Space THz Technology, 400
Liu, X., Guo, W., Wang, Y., et al. 2017, Appl. Phys. Lett., 111, 252601
Marting, L. H., Karatsu, K., Endo, A., Baselmans, J. J. A., & Pascual Laguna, A. 2024, J. Low Temp. Phys., 216, 144
Mirzaei, M., Barrentine, E. M., Bulcha, B. T., et al. 2020, in Proc. of Millimeter, Submillimeter, and Far-Infrared Detectors and Instrumentation for Astronomy X, 11453, eds. J. Zmuidzinas, & J.-R. Gao, International Society for Optics and Photonics (SPIE), 114530M
Moerman, A., Gafaji, M. H., Karatsu, K., & Endo, A. 2023, J. Open Source Softw., 8, 5478
Moerman, A., Karatsu, K., Yates, S. J. C., et al. 2024, A&A, 684, A161
Moerman, A., Karatsu, K., Baselmans, J. J. A., et al. 2025, J. Astron. Telesc. Instrum. Syst., 11, 025007
Neto, A. 2010, IEEE Trans. Antennas Propag., 58, 2238
Neto, A., Monni, S., & Nennie, F. 2010, IEEE Trans. Antennas Propag., 58, 2248
Nitta, T., Sekiguchi, S., Sekimoto, Y., et al. 2014, J. Low Temp. Phys., 176, 677
Pascual Laguna, A., Karatsu, K., Thoen, D., et al. 2021, IEEE Trans. Terahertz Sci. Technol., 11, 635
Paveliev, D. G., Koshurinov, Y. I., Ivanov, A. S., et al. 2012, Semiconductors, 46, 121
Rybak, M., Bakx, T., Baselmans, J. A., et al. 2022, J. Low Temp. Phys., 209, 766
Shu, S., Calvo, M., Goupy, J., et al. 2018, Appl. Phys. Lett., 113, 082603
Sunyaev, R. A., & Zeldovich, Y. B. 1970, Astrophys. Space Sci., 7, 3
Sunyaev, R. A., & Zeldovich, Y. B. 1980, MNRAS, 190, 413
Suzuki, A., Arnold, K., Edwards, J., et al. 2012, in Proc. of Millimeter, Submillimeter, and Far-Infrared Detectors and Instrumentation for Astronomy VI, 8452, ed. W. S. Holland, International Society for Optics and Photonics (SPIE), 84523H
Takaku, R., Cray, S., Aizawa, K., et al. 2026, Appl. Opt., 65, 4579
Takekoshi, T., Karatsu, K., Suzuki, J., et al. 2020, J. Low Temp. Phys., 199, 231
Taniguchi, A., Bakx, T. J. L. C., Baselmans, J. J. A., et al. 2022, J. Low Temp. Phys., 209, 278
Thoen, D. J., Bos, B. G. C., Haalebos, E. A. F., et al. 2017, IEEE Trans. Appl. Supercond., 27, 2631948
Thoen, D. J., Murugesan, V., Pascual Laguna, A., et al. 2022, J. Vac. Sci. Technol. B, 40, 052603
van Rantwijk, J., Grim, M., van Loon, D., et al. 2016, IEEE Trans. Microw. Theory Tech., 64, 1876
Yates, S. J. C., Baryshev, A. M., Yurduseven, O., et al. 2017, IEEE Trans. Terahertz Sci. Technol., 7, 789
Yates, S. J. C., Davis, K. K., Jellema, W., Baselmans, J. J. A., & Baryshev, A. M. 2020, J. Low Temp. Phys., 199, 156

[1] SRON – Space Research Organisation Netherlands, Niels Bohrweg 4, 2333 CA Leiden, The Netherlands
[2] Faculty of Electrical Engineering, Mathematics and Computer Science, Delft University of Technology, Mekelweg 4, 2628 CD Delft, The Netherlands
[3] Centro de Astrobiología (CAB), INTA-CSIC, Ctra. de Torrejón a Ajalvir km 4, 28850 Torrejón de Ardoz, Spain
[4] School of Physics and Astronomy, University of Minnesota/Twin Cities, 116 Church Street, SE, Minneapolis, MN 55455, USA
[5] Department of Cosmosciences, Graduate School of Science, Hokkaido University, Kita-10 Nishi-8, Kita-ku, Sapporo 060-0810, Japan
[6] National Astronomical Observatory of Japan (NAOJ), 2-21-1, Osawa, Mitaka, Tokyo 181-8588, Japan
[7] Institute of Astronomy, Graduate School of Science, The University of Tokyo, 2-21-1 Osawa, Mitaka, Tokyo 181-0015, Japan
[8] Research Center for the Early Universe, Graduate School of Science, The University of Tokyo, 7-3-1 Hongo, Bunkyo-ku, Tokyo 113-0033, Japan
[9] Kavli Institute for the Physics and Mathematics of the Universe (Kavli IPMU), The University of Tokyo, 5-1-5 Kashiwanoha, Kashiwa, Chiba, 277-8583, Japan
[10] Institute of Space and Astronautical Science, Japan Aerospace Exploration Agency (ISAS/JAXA), 3-1-1 Yoshinodai, Chuo-ku, Sagamihara, Kanagawa 252-5210, Japan
[11] Leiden Observatory, Leiden University, PO Box 9513, 2300 RA Leiden, The Netherlands
[12] Kitami Institute of Technology, 165 Koen-cho, Kitami, Hokkaido 090-8507, Japan
[13] Department of Physics, Graduate School of Science, Nagoya University, Furo-cho, Chikusa-ku, Nagoya, Aichi 464-8602, Japan
[14] Physikalisches Institut, Universität zu Köln, Zülpicher Straße 77, 50937 Cologne, Germany